Planetary and Space Science 238 (2023) 105796

Contents lists available at ScienceDirect

Planetary and Space Science

journal homepage: www.elsevier.com/locate/pss

A novel methodology to estimate pre-atmospheric dynamical conditions of small meteoroids

Erin C.M. Dawkins [a,b,*], Gunter Stober [c], Juan Diego Carrillo-Sánchez [a,b], Diego Janches [a], Robert Weryk [d], Jose Luis Hormaechea [e,f], Juan Sebastian Bruzzone [g], John M.C. Plane [h]

[a] ITM Physics Laboratory, NASA/Goddard Space Flight Center, Code 675, 8800 Greenbelt Rd., Greenbelt MD 20771, USA
[b] Department of Physics, Catholic University of America, 620 Michigan Ave., N.E. Washington, DC 20064, USA
[c] Institute of Applied Physics & Oeschger Center for Climate Change Research, Microwave Physics, University of Bern, Bern, Switzerland
[d] Physics and Astronomy, The University of Western Ontario, 1151 Richmond Street, London, ON, N6A 3K7, Canada
[e] Facultad de Ciencias Astronomicas y Geofisicas, Universidad Nacional de La Plata, Argentina
[f] Estacion Astronomica Rio Grande, Rio Grande, Tierra del Fuego, Argentina
[g] Facultad de Ciencias, Universidad de la República, Iguá 4225 Montevideo, Uruguay
[h] School of Chemistry, University of Leeds, Leeds, UK

ARTICLE INFO

Keywords:
Meteors
Meteor radars
Cosmic dust
Detection

ABSTRACT

Recent observations using the Wind and Ulysses spacecrafts and the Solar Occultation For Ice Experiment (SOFIE) during the period between 2007 and 2020 indicate a total cosmic dust influx at Earth ranging from 22 to 32 tonnes per day. Much is still unclear about the formation, evolution, and propagation of this cosmic dust throughout our Solar System, as well as the transport and chemical interaction of such particles within our own atmosphere. Studying meteoroids, which are particles small and fast enough to ablate in the Earth's upper atmosphere producing meteor plasma detectable by meteor radars, offers an opportunity to better understand these processes. While meteor radars provide a powerful tool to detect meteoroids, they are limited to detecting particles that produce a sufficient amount of plasma within the instrument's field-of-view, and thus most of their trajectory remains undetected. In this work, we report a novel methodology, using new polarization measurements as well as two state-of-the art models, to determine the pre-atmosphere dynamical characteristics of the detected particles, before they suffer any significant ablation or deceleration. We present the results for 20 meteor detection case studies, and find that for the majority of particles, at least 80% (typically 95%) of the particle mass has already been lost at the time of detection. In addition, while all particles experienced deceleration by the time of detection, this was typically small (≤4% of their initial velocity). Future work will implement this new methodology to automatically determine the initial mass and velocities of individual meteors. This will help provide more precise meteor orbits and characterization of parent source populations, as well as the identification of potential interstellar particles.

1. Introduction

Meteoroids with small enough diameters (between 100–1000 μm), and with sufficiently high entry velocities (11–72 km s^{-1}), burn up, or ablate, entirely in the Earth's upper atmosphere (80–120 km) due to friction with ambient air molecules (Öpik, 1958; McKinley, 1961; Plane, 2003). While some of the incoming meteoroid input is associated with meteor showers, the bulk is from a sporadic background not thought to be associated with any known meteor showers (Jones and Brown, 1993; Janches et al., 2009). Nevertheless, this sporadic meteoroid background can be assigned to astronomical dust source populations (radiant sources) traveling from six distinct directions relative to the Earth: the Helion and Anti-Helion, North and South Apexes, and the North and South Toroidal source populations (Jones and Brown, 1993; Campbell-Brown and Jones, 2006; Fentzke and Janches, 2008). The Helion and Anti-Helion sources are thought to primarily comprise of low-inclination and slower velocity Jupiter Family Comets (JFCs) traveling to or from the Sun's relative position (Nesvorný et al., 2010). The Apex sources primarily comprise of dust particles with much higher relative velocities (around 55 km s^{-1} Fentzke and Janches, 2008; Schult et al., 2017) from the Oort Cloud Comet (OCC), Halley Type Comets (HTC) and Asteroid (AST) populations [i.e., (OCC; Nesvorný et al., 2010, 2011; Pokorný et al., 2014)]. Finally, the North and South

* Corresponding author at: ITM Physics Laboratory, NASA/Goddard Space Flight Center, Code 675, 8800 Greenbelt Rd., Greenbelt MD 20771, USA.
E-mail address: erin.dawkins@nasa.gov (E.C.M. Dawkins).

https://doi.org/10.1016/j.pss.2023.105796
Received 5 June 2023; Received in revised form 14 September 2023; Accepted 6 October 2023
Available online 9 October 2023

Toroidal sources comprise of meteoroids at high ecliptic latitudes also originating from HTCs (Pokorný et al., 2014).

In previous decades, several authors provided a wide range of the total amount of cosmic dust entering the Earth's atmosphere from this sporadic background (between 3 and 270 t day^{-1}) (Plane, 2012). However, more recent work by Carrillo-Sánchez et al. (2020b) estimated that the global mass influx into the Earth's atmosphere is 28 ± 16 t day^{-1}, with contributions from JFCs, ASTs, and HTCs of 70%, 9%, and 21%, respectively. They found that JFCs are the main mass contributor to the total accreted mass, which is consistent with previous estimates (Zook, 2001; Nesvorný et al., 2010; Rowan-Robinson and May, 2013). Recently, observations using the Wind and Ulysses spacecrafts and the Solar Occultation For Ice Experiment (SOFIE) on board the AIM (Aeronomy of Ice in the Mesosphere) spacecraft, during the period between 2007 and 2020 (Hervig et al., 2022) indicate a total meteoric influx at Earth ranging from 22 to 32 t day^{-1}, in good agreement with the modeling results reported by Carrillo-Sánchez et al. (2020b,a) and other ground-based observations (Dunker et al., 2013).

Ground-based meteor radars offer a powerful tool with which to detect meteoroids entering the Earth's upper atmosphere. In this work we focus on specular meteor echos which are the radar signatures of the cylindrically diffusing plasma that is released from meteoroids along their trajectory as they undergo ablation. Such measurements have been performed since the late 1940s (Herlofson, 1947; Kaiser, 1953; Greenhow et al., 1982; Jacobi et al., 2007; Fritts et al., 2010a,b; Andrioli et al., 2013; Liu et al., 2013; De Wit et al., 2014; Chau et al., 2020; Stober et al., 2022). Meteor radars operate by transmitting shaped radio waves, which can reflect off a target with the returning echo detected by the radar receiver antenna. Arrays of receiver antennas can be used to apply interferometry to geolocate the echo and determine the time and altitude at which it is detected (Hocking et al., 2001). In some cases, using a Fresnel-diffraction pattern, the velocity of the particle can also be determined but not its direction of motion. With the addition of remote receiving stations separated from the transmitter by several km, spatio-temporal lags in the reflected signal from a single moving target can be detected, and from this, measurements of the particle trajectory can also be obtained (Webster et al., 2004; Janches et al., 2015; Bruzzone et al., 2021; Mazur et al., 2020).

However, a key limitation of meteor radars is that they can only detect particles which produce a sufficient amount of electrons while moving within the radar field-of-view, which implies that the particle has already undergone significant mass loss and deceleration at the time of detection. This requires a correction for deceleration to be applied to the measurements in order to obtain the initial velocity of the particle prior to entering the Earth's atmosphere. Current methodologies to perform such corrections use meteor shower knowledge and are difficult to apply to sporadic meteors on a case-by-case basis (Bruzzone et al., 2020; Stober et al., 2011; Schult et al., 2015). Obtaining accurate initial conditions of the particle at 500 km, prior to it entering the atmosphere, is critical to estimate precise orbital information. In addition, radars cannot provide meteoroid mass information, which is one of the most fundamental physical quantities, but still poorly constrained.

In this work, we present a new methodology that utilizes radar observations using the Southern Argentina Agile Meteor Radar Orbital System (SAAMER-OS) (Janches et al., 2019). This system provides altitude, velocity, and trajectory information for each meteor at the time of detection. In addition, with the introduction of two new antennas, the radar provides polarization measurements for each detected meteor. We use these observations in combination with two state-of-the art models: (1) a full-wave scattering model to determine, from the observations, a physically consistent solution to the electron line density q of the particle at the time of detection that satisfies Maxwell's equation, without additional assumptions or approximations based on analytical solutions of the radial cylindrical diffusion equation, and (2) a chemical ablation model that uses the measurements and q to estimate the initial conditions of each particle at 500 km altitude.

In the following section, we will describe the SAAMER-OS system and the new polarization measurement capability, as well as outline both models and describe how they are used in conjunction with the measurements to obtain each particle's initial conditions. Finally, we apply the methodology to 20 individual meteor detections as case studies.

2. Materials and methods

2.1. The Southern Argentina Agile Meteor Radar Orbital System (SAAMER-OS) meteor radar system

SAAMER-OS is located and hosted by the Estacion Astronomica Rio Grande in Tierra del Fuego (53.8°S, 67.8°W), at the southernmost tip of Argentina. First deployed in 2008 to measure winds in the mesosphere within one of the most atmospherically dynamic geographic regions on the planet, the system has been widely used to investigate mesospheric gravity waves within the southern Andes and Drake passage area (Fritts et al., 2010a; De Wit et al., 2016, 2017; Liu et al., 2013, 2017; Stober et al., 2021, 2022). In 2010 the SAAMER-OS system was initially augmented with two additional remote sites to determine meteoroid velocity and thus trajectories (including entry angle) (Janches et al., 2015), evolving over time to five passive remote receiver stations, each located at distances between 8–13 km from the transmitting station. From these measurements, meteoroid orbital determination is possible, and results from these observations, as well as a description of the system, can be found in Janches et al. (2015), Bruzzone et al. (2020), Bruzzone et al. (2021), and Panka et al. (2021). The system transmits 64 kW of peak power at 32.55 MHz and all antennas are three element crossed Yagis. The specular meteor observations are conducted using a single Yagi antenna for transmission with a full-width half maximum of 109^o. A full description of the SAAMER beam pattern can be found in Fritts et al. (2010b), although it should be noted that for this work, we have only used a single antenna.

In May 2022, another significant upgrade was made to the SAAMER-OS system, which is critical for this work: two additional passive receiver antennas were deployed next to the interferometer array at the main station. The antennas are wired to the receivers in such a manner that each one receives a separate polarization direction from the meteor trail backscattered electromagnetic wave, in contrast to the rest of the antennas which receive in a circularly polarized mode. Two examples of these new measurements are displayed in Fig. 1 showing the perpendicular degrees of polarization. With this addition, the system now provides orbital and polarization information for each of the 7000–15000 meteors detected daily.

From these new measurements, we obtain and utilize for this work the following quantities: (1) the altitude and time of detection, z_S and t_S, determined with the SAAMER-OS main station and its interferometer receiver array; (2) the velocity at the moment of detection and entry angles, v_S and α, derived from the trajectory obtained with the remote sites for orbital determination; and (3) the polarization information measured from the two new antennas described earlier. We then use these values as input to the full-wave scattering model first described by Stober et al. (2021), where quantitative analyses of transverse scatter meteors, detected using simultaneous triple-frequency meteor observations utilizing the Canadian Meteor Orbit Radar (CMOR), are made to derive physically consistent solutions of the ambipolar diffusion coefficient D, electron line density q, and initial trail radius r_0, along a cylindrical trail. In a companion paper to this manuscript, Stober et al. (2023) presented additional simulations of the transverse scatter meteor echo profiles for different background collision frequencies to account for the increase in ion-neutral and electron-neutral collisions over the altitude range where specular meteor trails are observed by radars (~75–110 km). Stober et al. demonstrated that utilizing the polarization information of a given echo produces a similar result to that of the triple-frequency

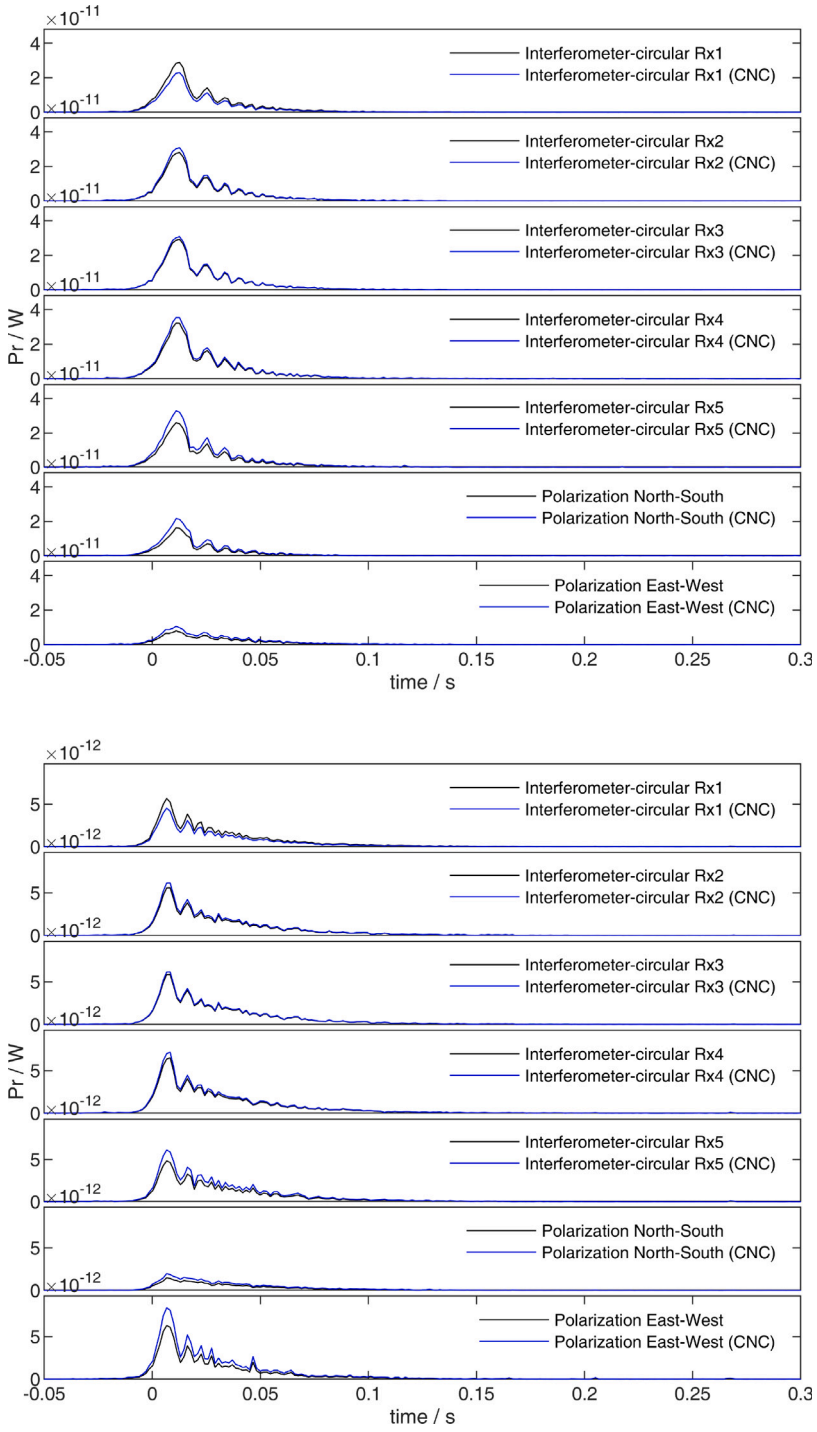

Fig. 1. Two examples of the new polarization measurements using the noise generator calibration and the cosmic noise calibration (CNC) described in the companion paper by Stober et al. (2023). The first five rows of each panel show the received power by each of the five interferometer antennas. The last two rows show the received signal in each polarization direction (North–South, East–West). As can be seen in these examples strong polarization effects are often present: in the first example there is a larger N–S component while in the second there is a much larger E–W component shown.

observations made using CMOR. Here, we simultaneously fit the full-wave scattering model to the circularly polarized SAAMER-OS return signal, as well as to the transverse and parallel polarized returns in order to derive D, q_S, and r_0 for each detected meteor for which we have orbital information.

The final step of our methodology involves estimating the mass of the meteoroid at the moment of detection (m_{EST}), and using it in combination with the measurements and the estimation of q_S to correct for deceleration and obtain the pre-atmospheric (i.e., at 500 km altitude) meteoroid mass, m_{INIT} and velocity, v_{INIT}, on a case-by-case basis. For this purpose, we utilize the most recent version of the University of Leeds Chemical Ablation Model (CABMOD) (Carrillo-Sánchez et al., 2020a).

2.2. The University of Leeds Chemical Ablation Model (CABMOD)

CABMOD simulates the ablation profile (as a function of altitude) of a meteoric particle of a particular composition, with an initial mass,

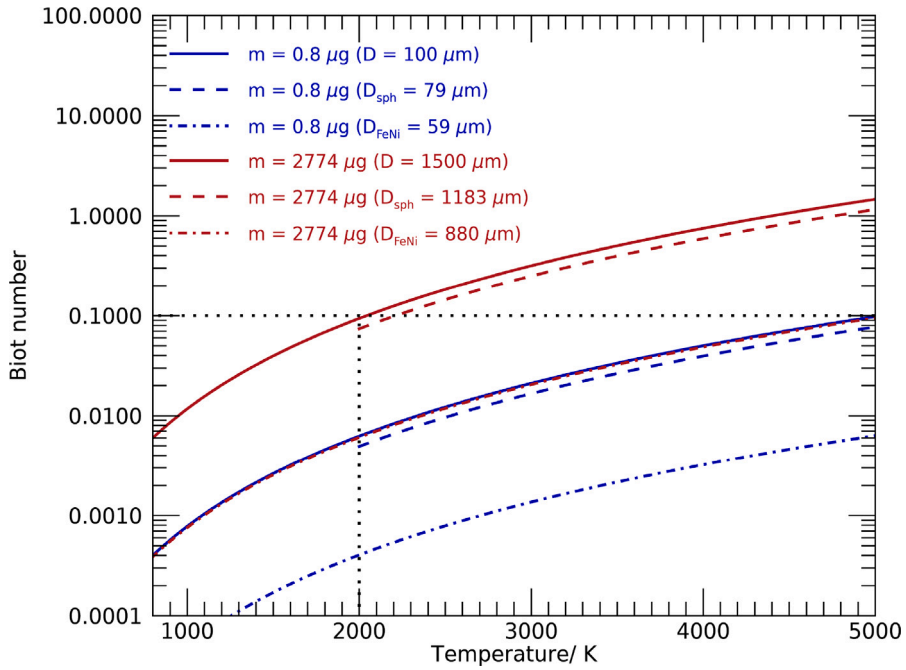

Fig. 2. Dependence of the Biot number, *Bi*, on the particle temperature for two masses 0.8 μg (in blue) and 2774 μg (in red), and both compositions, CI chondrites with inclusions of Fe–Ni metal grains (solid lines) and pure Fe–Ni bodies (dash-dotted lines). The filling in of pores and irregularities in the silicate phase may lead to a dramatic reduction of the particle diameter and, consequently, a decrease of *Bi* – this effect is illustrated by the dashed curves.

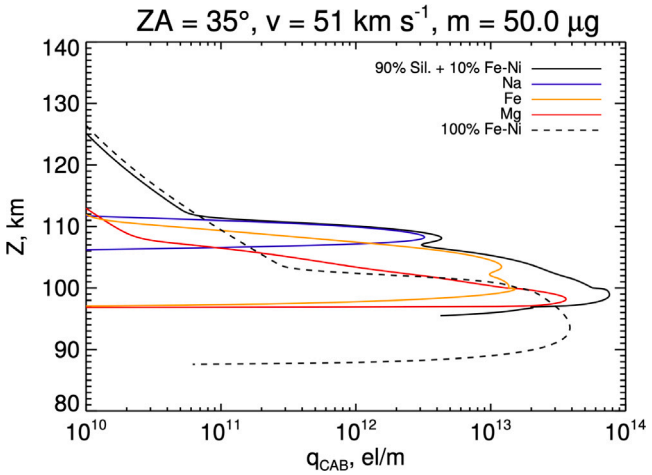

Fig. 3. Electron production rates, q_{CAB}, as a function of the altitude for an initial mass of 50 μg, an entry velocity of 51 km s^{-1}, and a zenith angle of 35°, and for two compositions — CI chondritic with metal Fe–Ni grains (solid black line) and pure Fe–Ni (dashed black line). In the case of a CI chondritic composition, volatile species such as Na (in blue) contribute to the electron production rates at higher altitudes than the main constituents, such as Fe (in orange) and Mg (in red).

velocity, and entry angle for a given season and latitude. The model extends across the altitude range 0–500 km, and results from the interpolation of the MSIS90 dataset (MSIS90) using altitude steps of 0.1 km. We produce a CABMOD library for 11 latitude bins (90°N to 90°S, in 20° intervals), across four seasons (March, June, September, and December), and for zenith angles between 0° and 90° (5° intervals). Initial pre-atmosphere geocentric velocities vary from 11 km s^{-1} (i.e., with the escape velocity of the Earth) to 72 km s^{-1} (Solar System escape velocity), with velocity steps of 2 km s^{-1}. We use a range of different initial meteoroid diameters (10, 20, 30, 50, 100, 200, 300, 400, 500, 600, 800, 1000, 1200, and 1500 μm), which correspond to particles with initial masses of 0.0008, 0.007, 0.02, 0.1, 0.8, 7, 22, 53, 103, 178, 421, 822, 1420, and 2774 μg, respectively, assuming a bulk density of 1570 kg m^{-3} (Flynn et al., 2018).

2.2.1. Assumed composition of meteoric particles

By default, the CABMOD model assumes that the elemental abundances of meteoric metals are defined by a Carbonaceous Ivuna (CI) composition (see Table 1, Lodders and Fegley, 2011), and it accounts for the ablation rates from both the silicate bulk (Vondrak et al., 2008) and the Fe–Ni metal grains (Carrillo-Sánchez et al., 2020b; Bones et al., 2019). Additionally, we have created a second library to model the ablation process of metallic grains with a purely Fe–Ni composition with 91.4 wt% in Fe and 8.6 wt% in Ni (Berger et al., 2016; Harries and Langenhorst, 2013), and with a bulk density of 7440 kg m^{-3} (Nawaby and Rochette, 2016). As discussed below, metallic bodies may ablate significantly lower than stony meteoroids within the upper atmosphere, and may also be detectable by the meteor radar beam. Note that both libraries are created only for particles with masses ≤ 2774 μg to ensure that the meteoroids heat isothermally, and to avoid differences in the composition and the chemical states of elements between the core and the skin of the particle. As discussed in Vondrak et al. (2008), if the dimensionless Biot number, *Bi*, is <0.1 (Kakac and Yener, 1985), an impinging meteoroid may be treated as isothermal. For a spherical body *Bi* is given by:

$$Bi = \frac{hR}{3k}$$

where h is the heat transfer coefficient in W m^{-2} K^{-1}, R is the radius in m, and k is the thermal conductivity in W m^{-1} K^{-1}. The heat transfer coefficient h can be expressed as:

$$h = \sigma T^3$$

where σ is the Boltzmann constant, and T is temperature in K. Fig. 2 shows the dependence of *Bi* on the particle temperature for two masses 0.8 μg (in blue) and 2774 μg (in red), and both compositions, CI chondrites with inclusions of Fe–Ni metal grains (solid lines) and pure Fe–Ni bodies (dash-dotted lines). In this study, we assume a value of k of 1.21 W m^{-1} K^{-1} for CI chondrites – k for a Carbonaceous Vigarano type

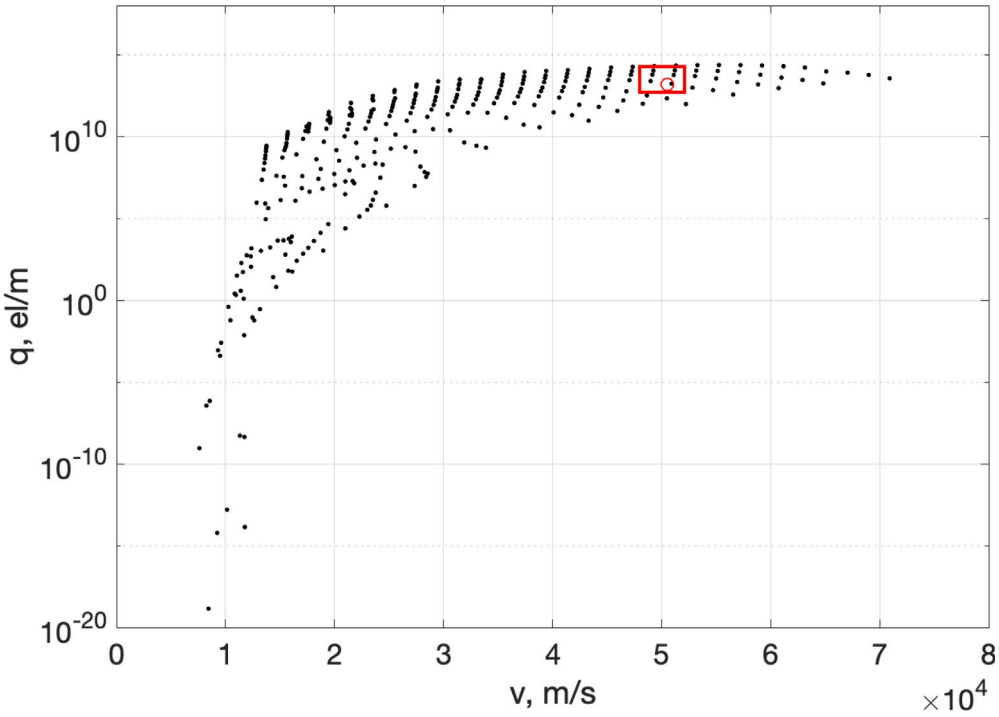

Fig. 4. All CABMOD velocity, v_{CAB}, versus electron line density, q_{CAB}, data points (black) at a given altitude best matching the altitude at which SAAMER-OS detected the particle. The red circle corresponds to the q_S and v_S estimated from SAAMER-OS. The red box indicates the subset of CABMOD simulated profiles that would be selected due to their vicinity to the SAAMER-OS estimate.

Table 1
Elemental atomic abundances normalized to Si and oxide mass in wt% for CI chondrites and measurements from the Cometary Secondary Ion Mass Analyzer/Rosetta mass spectrometer of dust particles, with diameters ranging from 50 to 1000 μm for the comet 67P/Churyumov-Gerasimenko.

Metal oxide	Carbonaceous Ivuna (CI)		Comet 67P/Churyumov-Gerasimenko	
	Elemental abundance	Oxide mass wt%	Elemental abundance	Oxide mass wt%
SiO_2	1	34.8	1	67.5
FeO(*silicate*)	0.60	25.1	0.29	23.1
Fe(*metal*)	0.27	8.6	–	–
MgO	1.03	24.0	0.11	5.2
CaO	0.060	2.0	5.43×10^{-3}	0.3
Al_2O_3	0.083	2.4	0.017	1.0
TiO_2	2.5×10^{-3}	0.11	–	–
Na_2O	0.057	1.0	0.08	2.8
K_2O	3.7×10^{-3}	0.10	2.11×10^{-3}	0.1
Ni	0.048	1.6	–	–
P_2O_5	8.2×10^{-3}	0.34	–	–

3 (CV3) meteorite – and 10.97 W m^{-1} K^{-1} for a Fe–Ni composition – iron meteorites III AB - (Soini et al., 2020). According to Fig. 2, particles with masses of 2774 μg stay isothermal for temperatures approximately up to 2000 K for a stony composition, whereas large metal bodies may be considered isothermal up to a very high temperature. Note that the ablation process may lead to a reduction of *Bi* for temperatures above 2200 K because of loss of the main chemical constituents (Gómez Martín et al., 2017). Additionally, once stony meteoroids melt during thermal ablation, the filling in of pores and irregularities in the silicate phase may lead to a dramatic reduction of the particle diameter and, consequently, a decrease of *Bi* – this effect is illustrated by the dashed curves in Fig. 2, assuming a spherule density of 3200 kg m^{-3} (Kohout et al., 2014).

2.2.2. Estimation of vertical profiles of electron line density

The CABMOD model can be used to estimate the vertical profiles of the electron line density, q_{CAB}. The ionization probability of meteoric metals for ionizing collisions with air molecules has been discussed in several studies (DeLuca et al., 2018; Janches et al., 2017), where the ionization efficiency for a given metal X, $\beta_{0X}(V)$, can be expressed as a function of the impact velocity V:

$$\beta_{0X}(V) = \frac{c_X \left(V - V_{0X}\right)^2 V^{0.8}}{1 + c_X \left(V - V_{0X}\right)^2 V^{0.8}}$$

where V_{0X} is the threshold velocity needed to start the ionization of metal X, given by:

$$V_{0X} = \sqrt{\frac{2\left(M_X + M_a\right) e\psi_X}{M_X M_a}}$$

where M_X and ψ_X are the mass and first ionization potential of the meteoric chemical species (X = Na, K, Fe, Mg, Si, Ca, Al, Ti, P, Ni, and O), respectively, e is the electronic charge, and M_a is the molecular weight of the air at typical ablation altitudes. According to the MSIS90 model, the ratio (atoms N_2):(atoms O_2) is practically constant below 100 km of altitude and, therefore, in this study we consider a constant value of M_a of 0.02896 kg mol^{-1}. Finally, c_X is a fitted parameter which is calculated relative to that for the collisional ionization of Fe (for X = Na, K, Mg, Si, Ni, P, and O) and Al (for the more refractory species,

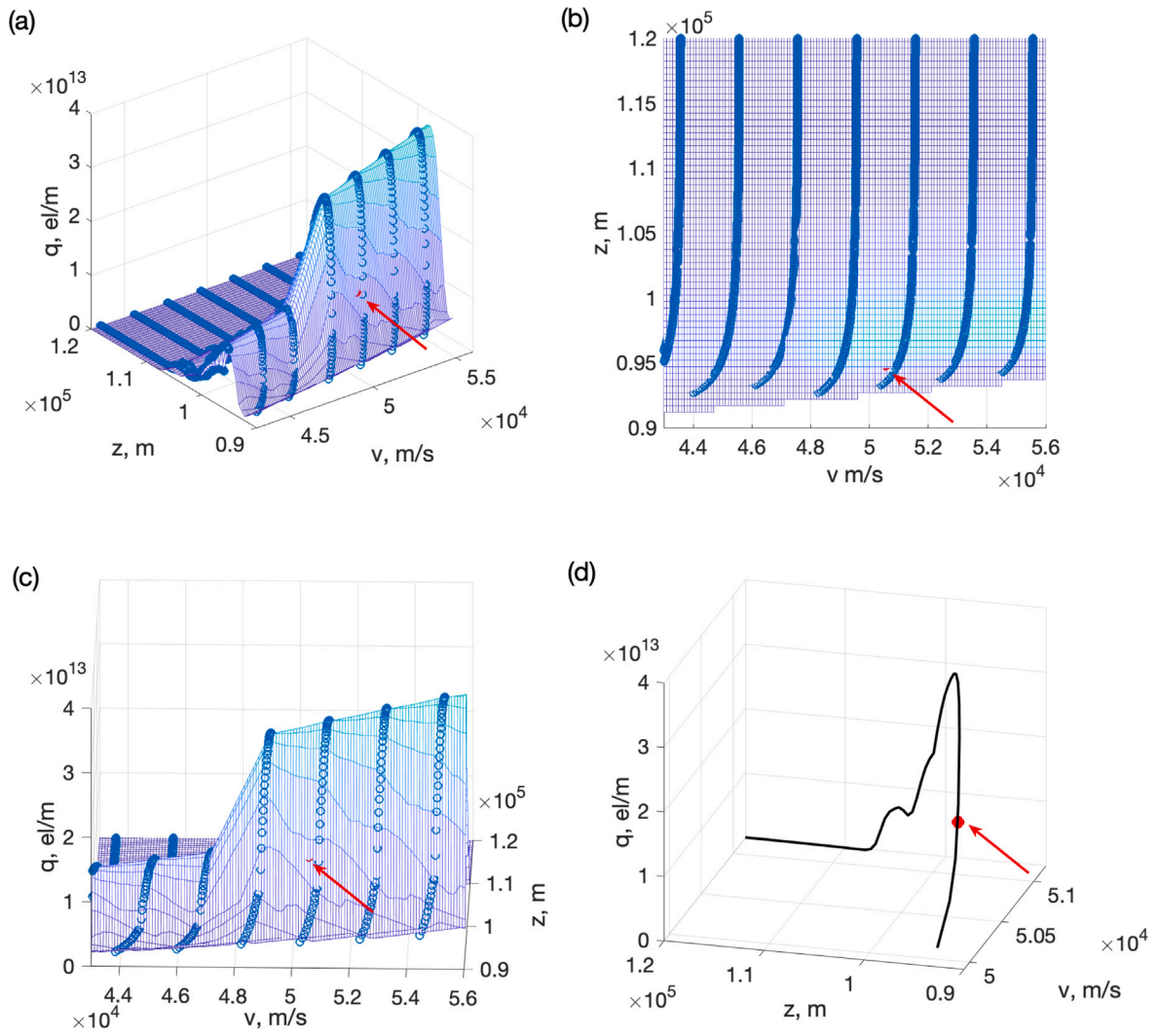

Fig. 5. Example of 3-D interpolation between a subset of CABMOD profiles (v, q, z) that are in the vicinity of the SAAMER-OS detection. Panels (a–c) present three different views of the 3-D interpolation between the subset of CABMOD profiles (blue circles). The SAAMER-OS estimate is indicated by the red filled circle, and further highlighted by the red arrows. Panel (d) shows the full interpolated profile that best corresponds to the SAAMER-OS estimate. For the sake of illustrative clarity, only an altitude range between 90–120 km is presented.

that is, X = Ca and Ti), respectively:

$$c_X = c_{Fe/Al}\left[\frac{\psi_{Fe/Al}}{\psi_X}\right]^2$$

For Fe in air, $c_{Fe} = 1.95 \times 10^{-4} \pm 0.03 \times 10^{-4}$ (km s^{-1})$^{2.4}$ and $V_{0Fe} = 8.94$ km s^{-1}; and for Al in air, $c_{Al} = 1.60 \times 10^{-4} \pm 0.03 \times 10^{-4}$ (km s^{-1})$^{2.4}$ and $V_{0Al} = 9.09$ km s^{-1} (DeLuca et al., 2018). Jones (1997) introduces a correction to $\beta_{0X}(V)$ to consider the possibility that ionization does not occur on the first collision and, instead, it may occur on a subsequent collision:

$$\beta_X^{ip}(V) = \beta_{0X}(V) + 2\int_{V_{0X}}^{V}\frac{\beta_{0X}(V')}{V'}dV'$$

According to DeLuca et al. (2018), the ionization efficiency for a metal X, $\beta_X^{ip}(V)$, can be fitted with the following equation:

$$\beta_X^{ip}(V) = \frac{c_X\left(V - V_{0X}\right)^n V^{0.8}}{1 + c_X\left(V - V_{0X}\right)^n V^{0.8}}$$

where $n = 1.6$. Fig. 3 shows the electron production rates, q_{CAB}, as a function of the altitude for an initial mass of 50 μg and an entry velocity of 51 km s^{-1} for two compositions — CI chondritic with metal Fe–Ni grains (solid black line) and Fe–Ni (dashed black line). In the case of a CI chondritic composition, volatile species such as Na (in blue) contribute to the electron production rates at higher altitudes than the main constituents, such as Fe (in orange) and Mg (in red), with Mg being the main contributor to the overall electron production rates. It is important to note that the CABMOD model predicts that the pure Fe–Ni meteors peak 10 km lower.

There are three main sources of uncertainty in the CABMOD model which may affect the value of q_{CAB}. Firstly, as discussed above, the CABMOD model considers the elemental atomic abundances of CI chondrites for all the chemical constituents (see Table 1; Lodders and Fegley, 2011) and, therefore assumes the stony bodies are mineralogically and compositionally equivalent to the primitive nebular condensate. However, in reality, cometary particles may exhibit relative enrichment or depletion of the elemental atomic abundances compared to primitive CI chondrites. The Cometary Secondary Ion Mass Analyzer/Rosetta mass spectrometer analyzed dust particles with diameters ranging from 50 to 1000 μm from 67P/Churyumov-Gerasimenko (67P), quantifying the elemental abundances for a wide number of samples (Bardyn et al., 2017). For example, Table 1 shows that the content of MgO in meteoroids from cometary origin is 5.2 wt%, that is, a factor of ~4.6 lower than for CI chondrites. A second source of uncertainty is the ionization efficiency of the meteoric metals: as discussed above, in the present study we have used the experimental parameters c_{Fe}

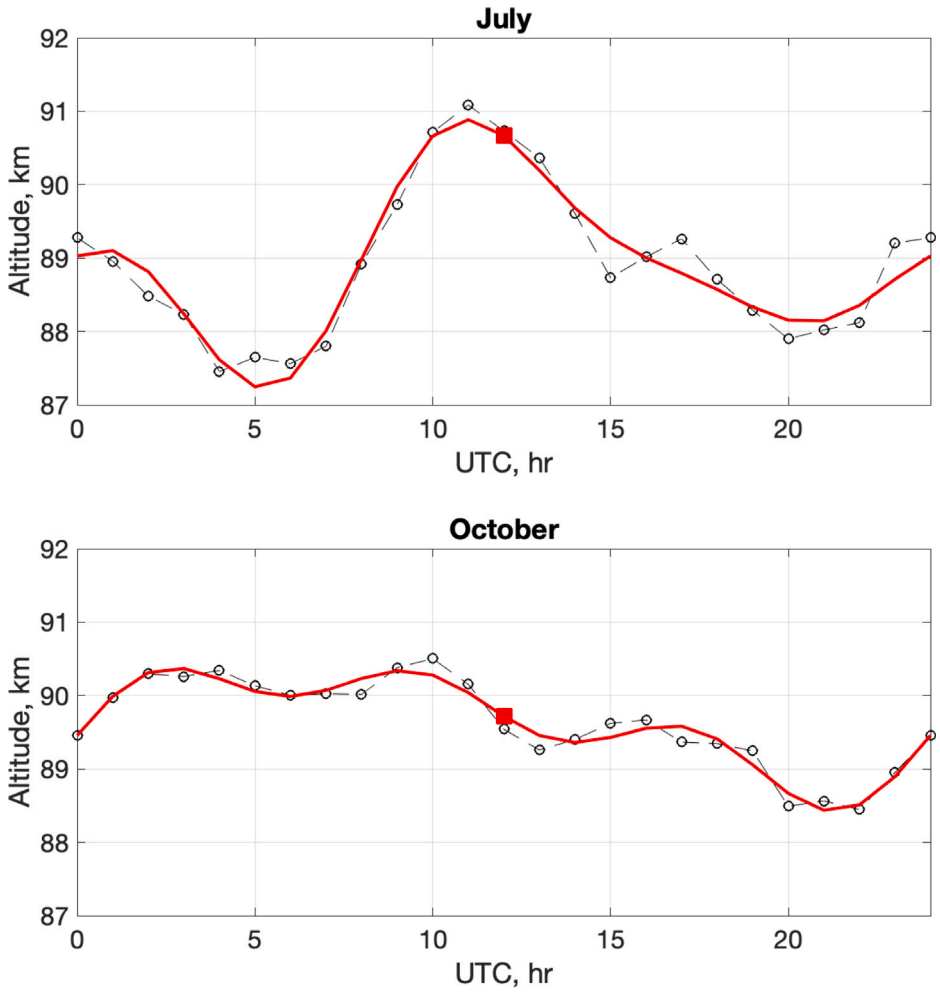

Fig. 6. Diurnal variation in the mean altitude of the meteor ablation distribution at the SAAMER-OS location for July and October. The data points (black circles) represent multi-year mean meteor ablation altitudes. The red profile is the fit to this data including diurnal, semidiurnal, and terdiurnal terms. The red square indicates the time at which CABMOD simulations are performed (12 UTC).

and c_{Al} to extrapolate the ionization yields for the remaining chemical compounds. Nonetheless, further studies are necessary to constrain the ionization yields of main constituents such as Mg. Finally, according to the University of Leeds Meteor Ablation Simulator (MASI) experimental results (Gómez Martín et al., 2017), the CABMOD model satisfactorily reproduces the measured peak ablation pulses from silicate – Fe, Na, P, and Ca – and metal Fe–Ni phases (Gómez Martín et al., 2017; Bones et al., 2019; Carrillo-Sánchez et al., 2020b,a). Nevertheless, although the CABMOD model can reproduce most of the ablation features of the Mg pulses measured by the MASI, it does not entirely capture the width of the Mg ablation profiles, due to the presence of different mineral phases which melt inhomogeneously. Consequently, the injection rate profiles of Mg estimated by the CABMOD model should be slightly broader to match the MASI observations (Bones et al., 2018).

2.3. Determination of pre-atmospheric dynamical parameters of detected particles

We initially select CABMOD vertical profiles of v_{CAB}, q_{CAB}, and m_{CAB}, which correspond to the latitude, season and entry angle α of the particular SAAMER-OS case study measured values. We then select a further subset of these CABMOD library files for where v_{CAB} and q_{CAB} lie within the vicinity of the SAAMER-OS v_S and estimated q_S, at the altitude at which SAAMER-OS detected the particle, z_S. An example of all CABMOD v_{CAB} and q_{CAB} values at an altitude consistent with z_S is presented in Fig. 4 (black data points), along with the SAAMER-OS estimated v_S and q_S (red circle). The data points within the red rectangle represent the subset of CABMOD profiles that are selected due to their proximity with the SAAMER-OS estimates. As discussed above, given the uncertainties of the CABMOD model, it may be necessary to reduce q_{CAB} by a certain factor such that there is overlap between q_{CAB} and q_S at z_S.

Using this subset of CABMOD profiles, we perform a three-dimensional (3-D) interpolation across these parameters in order to produce a best estimate of the full vertical profile that matches the measurements at the altitude at which SAAMER-OS detected the particle, z_S. An example of this 3-D interpolation is provided in Fig. 5; panels (a–c) show three different views of the same 3-D interpolation. The subset of CABMOD profiles are shown as the blue circles as a function of v (ms^{-1}), z (m), and q (el m^{-1}). The SAAMER-OS estimate is indicated by the red filled circle, emphasized by the red arrows. Panel (d) shows the full interpolated profile that best corresponds to the SAAMER-OS estimate. Following this, we can use this interpolated profile (and similar ones for the mass profile, not shown) to track the meteor flight to the top of the atmosphere and estimate its initial conditions, including its initial velocity and mass. The derived initial meteoroid velocity (v_{INIT}) and mass (m_{INIT}) can then be used for a more accurate estimation of meteoroid orbits.

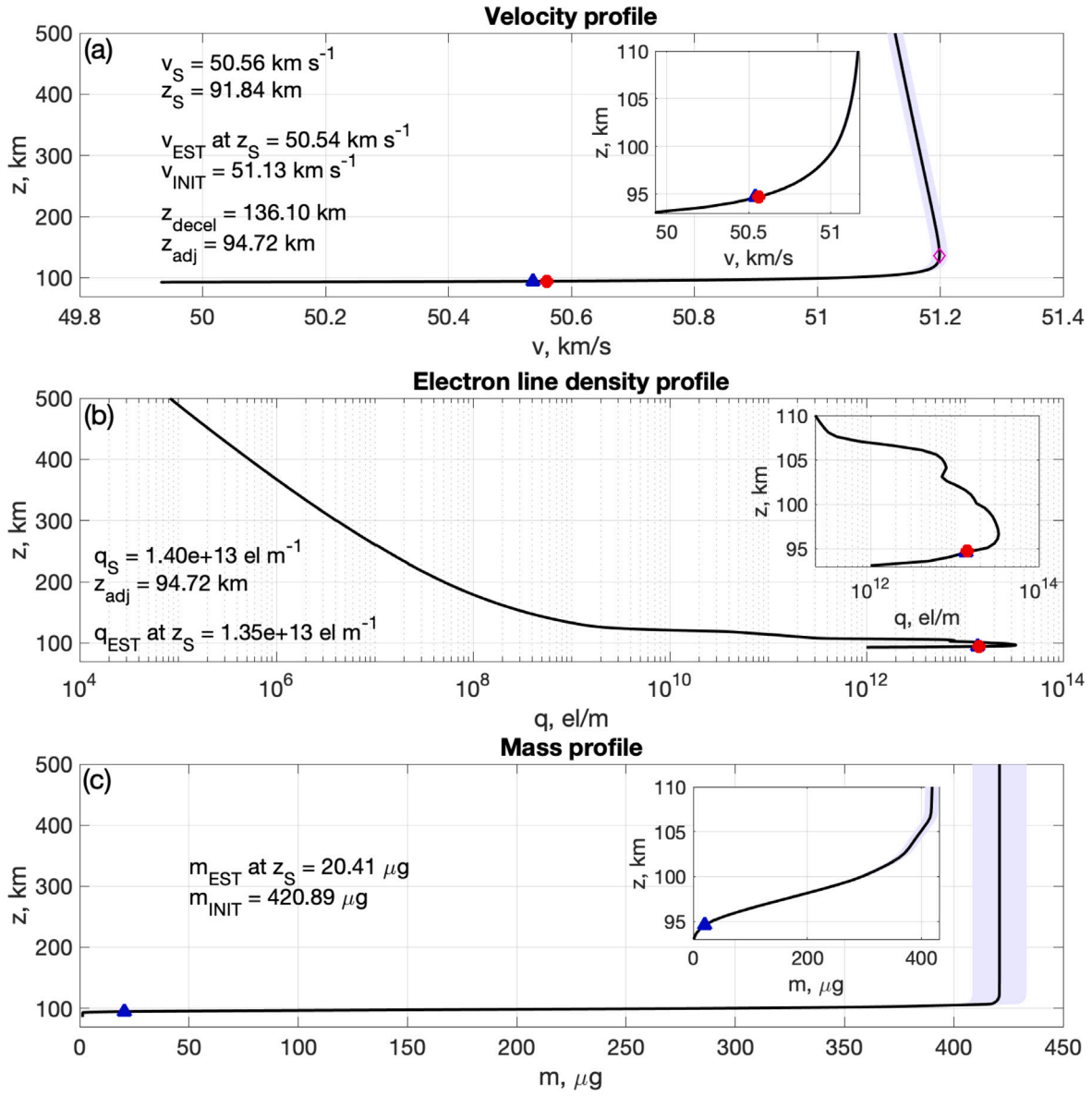

Fig. 7. Interpolated v, q, and m profiles for an example SAAMER-OS case study. Panel (a) presents the interpolated v profile as a function of z. The red filled circle corresponds to v_S, the magenta diamond indicates z_{decel}, the blue triangle indicates the estimated velocity at z_{adj}, denoted v_{EST}, and the initial velocity v_{INIT} is also noted. Panel (b) presents the interpolated q profile, where the x-axes are on a log scale. The red filled circle corresponds to q_S, while the blue triangle depicts the estimated q_{EST} at z_{adj}. Panel (c) shows the interpolated particle mass profile. The blue triangle indicates the estimated mass, m_{EST} at z_{adj}, while the mass at the top of the atmosphere, m_{INIT} is also noted. All panels include a subset panel which depicts the respective profile between 90–110 km. In each panel, the blue shaded region represents the 95% confidence interval.

3. Results and discussion

In order to develop and test our methodology we use 20 SAAMER-OS observations obtained between July 23rd–27th 2022, and October 20th–22nd 2022. These 20 case studies represent meteoroid particle detections from a range of detected velocities (between 21.11 km s^{-1} and 65.82 km s^{-1}) and local times. The CABMOD simulated profiles are determined at 12 UTC, but the time at which the 20 SAAMER-OS case studies were detected varies. Preliminary work has indicated that local time and seasonal variation does occur in the mean altitude of the bulk meteor ablation distribution at SAAMER-OS (see Fig. 6). The mean altitude is determined by producing a histogram of all SAAMER-OS individual meteor altitude detections for a given month, in order to find the peak maximum defined as the altitude at which the bulk of all individual meteors ablate (further described in Dawkins et al., 2023). It is important to consider this diurnal and seasonal variation when comparing each of the 20 SAAMER-OS case studies (all obtained at different UTCs) and CABMOD simulations (12 UTC, indicated by red filled square in Fig. 6). We thus correct the SAAMER-OS measured altitude to that which would correspond to 12 UTC. The corrected altitude is given by z_{adj} = diurnal fit(t_S) / diurnal fit(t_{CAB}) × z_S, where t_S is the UTC hour of the SAAMER-OS detection, t_{CAB} equals 12 UTC, and z_S is the SAAMER-OS detection altitude. We obtained z_{adj} values for each of the 20 SAAMER-OS case studies (mean altitude adjustment of 0.70 km, with maximum of 2.85 km).

Figs. 7 and 8 show two example case studies of our methodology. In Fig. 7a, the interpolated velocity profile is visualized as a function of altitude between 70–500 km and the measured v_S by SAAMER-OS is shown as a red filled circle. As can be seen from the particle trajectory, the particle enters the atmosphere at an initial top-of-the-atmosphere (TOA) velocity of v_{INIT}=51.13 km s^{-1} and continues to accelerate due to gravitational attraction until it encounters enough ambient air molecules to cause deceleration (z_{decel}=136.10 km, indicated by the magenta diamond). The particle continues to decelerate at

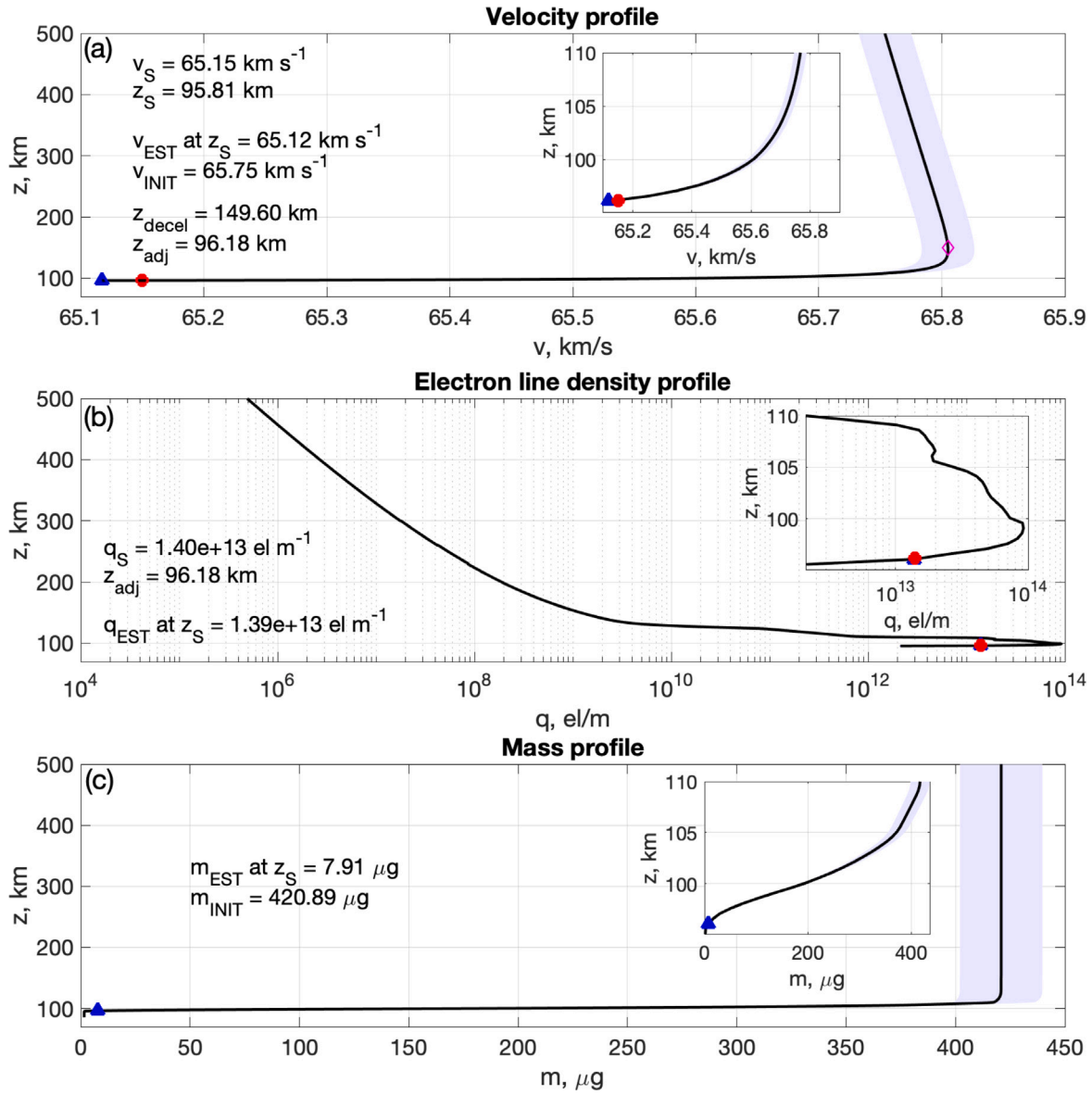

Fig. 8. Interpolated v, q, and m profiles for a second example SAAMER-OS case study with a faster velocity. Panel (a) presents the interpolated v profile as a function of z. The red filled circle corresponds to v_S, the magenta diamond indicates z_{decel}, the blue triangle indicates the estimated velocity at z_{adj}, denoted v_{EST}, and the initial velocity v_{INIT} is also noted. Panel (b) presents the interpolated q profile, where the x-axes are on a log scale. The red filled circle corresponds to q_S, while the blue triangle depicts the estimated q_{EST} at z_{adj}. Panel (c) shows the interpolated particle mass profile. The blue triangle indicates the estimated mass, m_{EST} at z_{adj}, while the mass at the top of the atmosphere, m_{INIT} is also noted. All panels include a subset panel which depicts the respective profile between 90–110 km. In each panel, the blue shaded region represents the 95% confidence interval.

a significantly increasing rate as it descends to lower altitudes. Fig. 7b and 7c present the best estimates for the interpolated q and m profiles as a function of altitude. One can see that by the time the particle is detected by SAAMER-OS, it has lost the majority of its initial mass. For all panels, 95% confidence intervals are provided; these are determined from Monte Carlo method sampling of the original SAAMER-OS v_S, z_S, and q_S estimates (1000 iterations), adding normally distributed artificial noise with σ values corresponding to ±0.5 km s^{-1}, ±0.1 km, and ±10%, respectively.

A summary of the results for the 20 individual SAAMER-OS case studies is presented in Fig. 9. Panel 9a depicts the estimated mass at z_{adj} versus the corresponding estimated initial mass at the TOA for each of the 20 case studies. One can see the initial particle mass range for the 20 case studies varies between 6.58 μg and 863.42 μg, fulfilling the isothermal conditions shown in Fig. 2. Irrespective of the initial particle mass, one can also see that the majority of particles have lost considerable mass by the time of detection. Fig. 9b shows that this mass loss is at least 80% (typically around 95%), of the initial mass for the majority of cases. This is supported by the results of Weryk and Brown (2012) which showed the radar specular/observation point to be preferentially offset towards the end of the corresponding video light curve for simultaneous radar-video meteor observations. Fig. 10 shows the mass ablated fraction of meteoroids estimated by the CABMOD model as a function of the initial mass and entry velocity, and with a fixed zenith angle of 35° for the atmospheric conditions of June. The modeling results indicate that larger particles ablate more efficiently even at lower velocities.

Panels 9c and 9d show that most particles, despite the significant mass loss, have only experienced minimal deceleration at the time of detection. Consistent with the findings of Plane (2003) one can see that faster particles typically ablate, and thus become detectable by SAAMER-OS, higher up in the atmosphere, whereas slower particles ablate at lower altitudes. Similarly, panel 9e shows that for the same initial mass range, particles with higher initial velocities typically

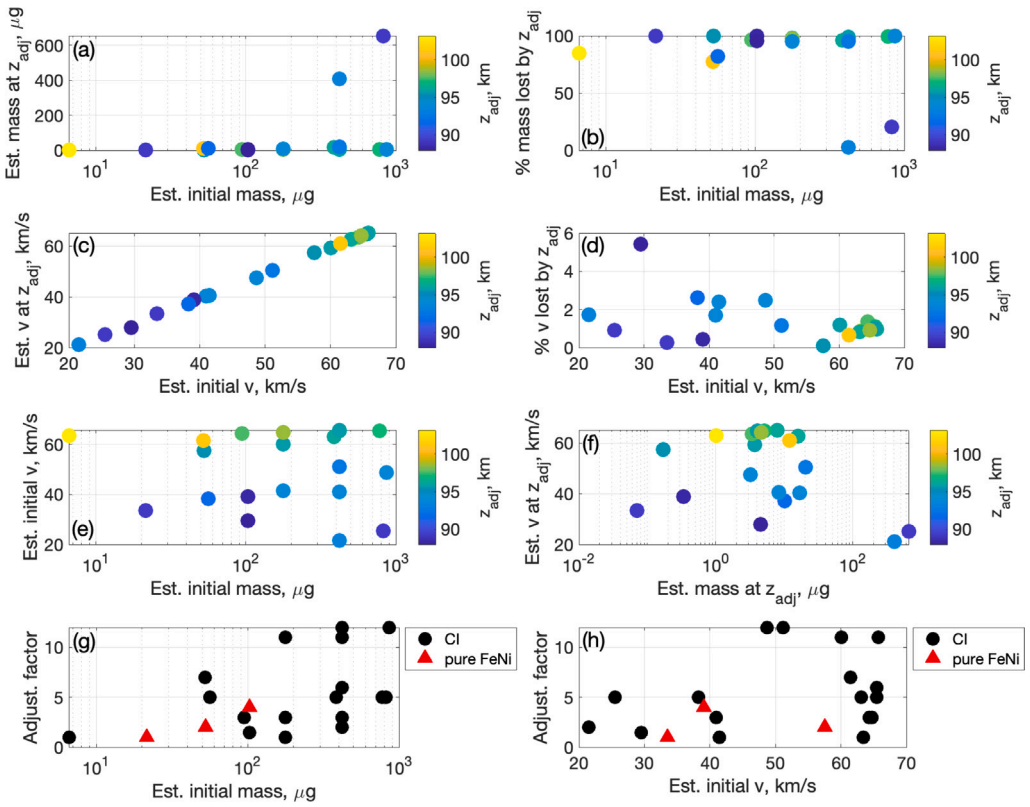

Fig. 9. Overview of results for the 20 case studies analyzed. Panel (a) presents the estimated mass of the particle at the respective z_{adj} versus the initial estimated mass of the same particles, while panel (b) presents the percentage of initial mass lost at the time of detection compared to the initial particle mass. Panel (c) presents the detected v versus the initial v, while panel (d) presents the percentage v lost at detection. Panel (e) presents the initial mass versus initial v, while panel (f) presents the estimated mass versus estimated v of the particle at the time of detection. For panels (a)–(f), the data points are color-coded according to z_{adj}. Panel (g) presents the adjustment factor for which q_{CAB} must be reduced by to ensure that there is overlap between q_{CAB} and q_S at z_S versus the initial estimated mass of the particles, while panel (h) presents the adjustment factor as a function of initial estimated v. For both panels (g) and (h), the data points are color-coded depending upon the likely particle composition: chondritic/CI (black filled circle) versus pure Fe–Ni (red filled triangle).

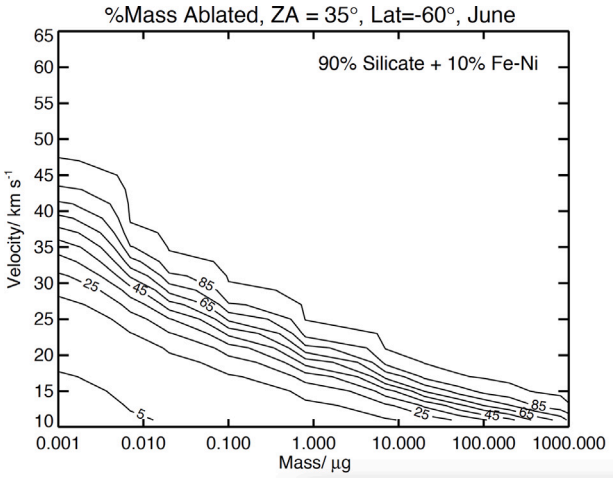

Fig. 10. Mass ablated fraction of meteors estimated by the CABMOD model as a function of the initial mass and entry velocity, with a fixed zenith angle of 35° for the atmospheric conditions of June.

ablate (and become detectable by SAAMER-OS) at higher altitudes, compared to lower velocity particles. Panel 9f is analogous to 9e, but this time for the detected velocity versus mass. In panel 9b, it should be noted that there are two case studies in which less than 25% of the initial particle mass has been lost at the time of detection. While both of these associated particles have the largest initial masses out of the 20 case studies, they also have the slowest initial estimated velocities, with initial velocities of <26 km s^{-1} (as in panels 9e and 9f), and thus we can see that these two slowest particles still preserve most of their initial mass at the time of detection.

4. Summary and conclusions

In order to determine precise orbital elements of meteoroids from ground-based meteor observations it is critical to correct for deceleration since, at the time of observation, the particle parameters may have significantly changed their initial conditions on entry (as shown in this manuscript). To date, methodologies to correct for deceleration are mostly limited to meteor showers using empirical methodologies on a general basis, and not for an individual meteor observation (Stober et al., 2011). For example, video observations using the Cameras for All-Sky Meteor Surveillance (CAMS) incorporates a deceleration correction as part of its reduction pipeline based on empirical equations reported by Whipple and Jacchia (1957) and Jacchia and Whipple (1961). Likewise, radar observations with CMOR and SAAMER-OS, use an empirical deceleration correction first described by Brown et al. (2004) to obtain an estimate of the true out-of-atmosphere meteoroid speed distribution. This methodology, also described in detail by Bruzzone et al. (2020), uses a large meteor orbit dataset, selecting meteors belonging to ~10 strong meteor showers and performing a first-order fit to the distribution of meteor speeds as a function of height for each shower selected. They recorded the height at which the linear fit

matches the reference geocentric speed of the shower, the slope of the linear fit, and the number of meteors utilized in the fit. The intersection height is assumed to be the height at which no deceleration has yet occurred. Repeating this procedure for each shower, a list of intersection heights, slopes, reference geocentric speeds, and the number of meteors is compiled. A linear fit of the slopes versus speeds and intersection heights versus speeds weighted by the number of meteors extracted in each shower is then performed to obtain a general correction factor. This technique thus has limited accuracy as it generalizes the problem, and it is only applicable to meteor showers for which the geocentric velocity is known.

To date, there are no reported methodologies that consider meteor observations on a case-by-case basis. In this work, we present a state-of-the-art methodology to determine the initial conditions of small meteoroids (i.e., velocity and mass), from both showers and the sporadic background, at the top of the atmosphere. This method utilizes a combination of meteor radar orbital and novel polarization measurements, and the most comprehensive models to date of the full-wave electromagnetic scattering of meteor trails and the ablation process. This is possible thanks to the recent upgrades to the SAAMER-OS system which enable simultaneous measurements of the echo return polarization, in addition to estimates of the entry angle, velocity and altitude of every detected meteor.

For this study, we focus on 20 individual SAAMER-OS detection case studies and we found that, in almost all cases, the particles had lost >80% of their mass before being detected by SAAMER-OS. All particles experienced deceleration at the time of detection compared to their initial velocities at the top-of-the atmosphere, although this was typically small (≤4%). Although the CABMOD model assumes a default CI chondrite composition, we found that 3 out of the 20 case studies could only be explained using the CABMOD model with an assumed pure Fe–Ni composition, that is, 15% of the total events. Even though the flux of iron meteoroids represents ~5% of the overall cosmic dust input (Zolensky et al., 2006), the CABMOD model estimates that these bodies ablate around 10 km lower than stony meteors and, consequently, enable detection by the meteor radar beam and thus potentially cause an overrepresentation of these cases in our sample population. Given the uncertainties of the CABMOD model, we found that it was necessary to reduce q_{CAB} for 18 out of the 20 case studies in order to match q_S, using factors typically ranging between 2 to 5. A maximum factor of 11 or 12 was used in 3 case studies. This reduction factor for q_{CAB} is probably associated with the depletion of the elemental atomic abundances of the main metals, such as Mg, compared to a typical CI chondrite composition and, additionally, an over-estimation of the ionization yields of some of the ablated meteoric compounds. Therefore, further future analysis is necessary to constrain the ionization yields of meteoric metals.

Ongoing work will focus on optimizing the processing code to maximize processing efficiency. Currently the altitude correction for the height of the detected meteoroid is determined according to the mean data obtained from SAAMER-OS observations. A future improvement would be to determine this atmospheric altitude correction from a physical atmosphere model, such as MSIS90, with a time resolution of an hour or less. Once streamlined, we plan to automate the processing to allow for rapid and near real-time processing of individual SAAMER-OS measurements. Once enabled, we will be able to automatically determine the initial mass and velocities for every meteor for which we can determine orbits. This will help provide more precise meteor orbits and characterization of parent source populations, as well as the identification of potential interstellar particles, and further constrain the total amount of cosmic dust input entering the Earth's atmosphere.

CRediT authorship contribution statement

Erin C.M. Dawkins: ECMD oversaw the preparation of the manuscript and implemented the methodology and data analysis throughout the document. Support for DJ, ECMD, JDCS as well as SAAMER-OS' operation are provided by NASA's Planetary Science Division Research Program, through ISFM work package Exospheres, Ionospheres, Magnetospheres Modeling at Goddard Space Flight Center and NASA Engineering Safety Center (NESC) assessment TI-17-01204. This work was supported in part by the NASA Meteoroid Environment Office under cooperative agreement no. 80NSSC18M0046. All authors discussed the results and edited the manuscript. **Gunter Stober:** GS performed the full-wave scattering simulations which permitted the derivation of important parameters necessary for this work. In addition he provided invaluable feedback, expertise and comments to the manuscript throughout its creation. GS is a member of the Oeschger Center for Climate Change Research (OCCR). Calculations were performed on UBELIX (http://www.id.unibe.ch/hpc, last access: 04 May 2023), the HPC cluster at the University of Bern. All authors discussed the results and edited the manuscript. **Juan Diego Carrillo-Sánchez:** JDCS performed and contributed the CABMOD simulations, and provided expertise and support on the use of CABMOD data. Support for DJ, ECMD, JDCS as well as SAAMER-OS' operation are provided by NASA's Planetary Science Division Research Program, through ISFM work package Exospheres, Ionospheres, Magnetospheres Modeling at Goddard Space Flight Center and NASA Engineering Safety Center (NESC) assessment TI-17-01204. This work was supported in part by the NASA Meteoroid Environment Office under cooperative agreement no. 80NSSC18M0046. All authors discussed the results and edited the manuscript. **Diego Janches:** DJ and RW had conceptualized the idea of polarization measurements on SAAMER and DJ is responsible for the operation and coordination of the system. DJ provided invaluable feedback, comments and expertise throughout the generation of this manuscript. Support for DJ, ECMD, JDCS as well as SAAMER-OS' operation are provided by NASA's Planetary Science Division Research Program, through ISFM work package Exospheres, Ionospheres, Magnetospheres Modeling at Goddard Space Flight Center and NASA Engineering Safety Center (NESC) assessment TI-17-01204. This work was supported in part by the NASA Meteoroid Environment Office under cooperative agreement no. 80NSSC18M0046. All authors discussed the results and edited the manuscript. **Robert Weryk:** DJ and RW had conceptualized the idea of polarization measurements on SAAMER and RW computed all orbital parameters and selected the meteors. RW is supported by the Pan-STARRS survey of the Institute for Astronomy at the University of Hawaii. All authors discussed the results and edited the manuscript. **Jose Luis Hormaechea:** JLH oversees the daily operation of the SAAMER-OS, and provided support for data acquisition vital for this work. All authors discussed the results and edited the manuscript. **Juan Sebastian Bruzzone:** JSB contributed analysis of orbital data which was critical to obtain the angular information fundamental for this effort. All authors discussed the results and edited the manuscript. **John M.C. Plane:** JMCP provided expertise on CABMOD, as well as invaluable feedback and insight on the results during the production of the manuscript. All authors discussed the results and edited the manuscript.

Declaration of competing interest

The authors declare that they have no known competing financial interests or personal relationships that could have appeared to influence the work reported in this paper.

Data availability

Data will be made available on request.

Acknowledgments

Support for DJ, ECMD, JDCS as well as SAAMER-OS' operation are provided by NASA's Planetary Science Division Research Program, through ISFM work package Exospheres, Ionospheres, Magnetospheres Modeling at Goddard Space Flight Center and NASA Engineering Safety Center (NESC) assessment TI-17-01204. This work was supported in part by the NASA Meteoroid Environment Office under cooperative agreement no. 80NSSC18M0046.

GS is a member of the Oeschger Center for Climate Change Research (OCCR).

Calculations were performed on UBELIX (http://www.id.unibe.ch/hpc, last access: 04 May 2023), the HPC cluster at the University of Bern.

RW is supported by the Pan-STARRS survey of the Institute for Astronomy at the University of Hawaii. All authors approved the version of the manuscript to be published.

References

Andrioli, V.F., Fritts, D.C., Batista, P., Clemesha, B., 2013. Ann. Geophys. 31 (5), 889–908. http://dx.doi.org/10.5194/angeo-31-889-2013.

Bardyn, A., Baklouti, D., Cottin, H., et al., 2017. Mon. Not. R. Astron. Soc. 469, S712–S722. http://dx.doi.org/10.1093/mnras/stx2640.

Berger, E.L., Lauretta, D.S., Zega, T.J., Keller, L.P., 2016. M&PS 51 (10), 1813–1829. http://dx.doi.org/10.1111/maps.12721.

Bones, D.L., Carrillo-Sánchez, J.D., Kulak, A.N., Plane, J.M.C., 2019. Planet. Space Sci. 179, 104725. http://dx.doi.org/10.1016/j.pss.2019.104725.

Bones, D.L., Gómez Martín, J.C., Carrillo Sánchez, J.D., Dobson, A.J., Plane, J.M.C., 2018. Geophys. Res. Lett. 45 (15), 7765–7771. http://dx.doi.org/10.1029/2018GL077427.

Brown, P., Jones, J., Weryk, R.J., Campbell-Brown, M.D., 2004. Earth Moon Planets 95, 617–626. http://dx.doi.org/10.1007/s11038-005-5041-1.

Bruzzone, J.S., Janches, D., Jenniskens, P., Weryk, R., Hormaechea, J.L., 2020. Planet. Space Sci. 188, 104936. http://dx.doi.org/10.1016/j.pss.2020.104936.

Bruzzone, J.S., Weryk, R.J., Janches, D., et al., 2021. Planet. Sci. J. 2 (2), 56. http://dx.doi.org/10.3847/PSJ/abe9af.

Campbell-Brown, M.D., Jones, J., 2006. Mon. Not. R. Astron. Soc. 367, 709–716. http://dx.doi.org/10.1111/j.1365-2966.2005.09974.x.

Carrillo-Sánchez, J.D., Bones, D.L., Douglas, K.M., et al., 2020a. Planet. Space Sci. 187, 104926. http://dx.doi.org/10.1016/j.pss.2020.104926.

Carrillo-Sánchez, J.D., Gómez-Martín, J.C., Bones, D.L., et al., 2020b. Icarus 335, 113395. http://dx.doi.org/10.1016/j.icarus.2019.113395.

Chau, J.L., Urco, J.M., Vierinen, J., Harding, B.J., et al., 2020. Earth Space Sci. 8 (1), e2020EA001293. http://dx.doi.org/10.1029/2020EA001293.

Dawkins, E., Stober, G., Janches, D., et al., 2023. Geophys. Res. Lett. 50 (2), e2022GL101953. http://dx.doi.org/10.1029/2022GL101953.

De Wit, R.J., Hibbins, R., Espy, P.J., et al., 2014. Geophys. Res. Lett. 41 (13), 4745–4752. http://dx.doi.org/10.1002/2014GL060501.

De Wit, R.J., Janches, D., Fritts, D.C., Hibbins, R.E., 2016. Geophys. Res. Lett 43, 4049–4055. http://dx.doi.org/10.1002/2016GL068599.

De Wit, R., Janches, D., Fritts, D., Stockwell, R., Coy, L., 2017. Geophys. Res. Lett. 44 (2), 1182–1191. http://dx.doi.org/10.1002/2016GL072311.

DeLuca, M., Munsat, T., Thomas, E., Sternovsky, Z., 2018. Planet. Space Sci. 156, 111–116. http://dx.doi.org/10.1016/j.pss.2017.11.003.

Dunker, T., Hoppe, U.-P., Stober, G., Rapp, M., 2013. Ann. Geophys. 31 (1), 61–73. http://dx.doi.org/10.5194/angeo-31-61-2013.

Fentzke, J.T., Janches, D., 2008. J. Geophys. Res. (Space Phys.) 113 (A03304), http://dx.doi.org/10.1029/2007JA012531.

Flynn, G.J., Consolmagno, G.J., Brown, P., Macke, R.J., 2018. Chemie der Erde (Geochemistry) 78 (3), 269–298. http://dx.doi.org/10.1016/j.chemer.2017.04.002.

Fritts, D., Janches, D., Hocking, W., 2010a. J. Geophys. Res.: Atmos. 115 (D19), http://dx.doi.org/10.1029/2010JD013891.

Fritts, D., Janches, D., Iimura, H., et al., 2010b. J. Geophys. Res.: Atmos. 115 (D18), http://dx.doi.org/10.1029/2010JD013850.

Gómez Martín, J.C., Bones, D.L., Carrillo-Sánchez, J.D., et al., 2017. Astrophys. J. 836 (2), 212. http://dx.doi.org/10.3847/1538-4357/aa5c8f.

Greenhow, M., Vinje, T., Brevig, P., Taylor, J., 1982. J. Fluid Mech. 118, 221–239. http://dx.doi.org/10.1017/S0022112082001050.

Harries, D., Langenhorst, F., 2013. M&PS 48 (5), 879–903. http://dx.doi.org/10.1111/maps.12089.

Herlofson, N., 1947. Nature 160 (4077), 867–868. http://dx.doi.org/10.1038/160867a0.

Hervig, M.E., Malaspina, D., Sterken, V., et al., 2022. J. Geophys. Res. (Space Phys.) 127 (10), e2022JA030749. http://dx.doi.org/10.1029/2022JA030749.

Hocking, W.K., Fuller, B., Vandepeer, B., 2001. J. Atmos. Solar Terr. Phys 63, 155–169. http://dx.doi.org/10.1016/S1364-6826(00)00138-3.

Jacchia, L.G., Whipple, F.L., 1961. Smithsonian Contrib. Astrophys. 4, 97–129.

Jacobi, C., Fröhlich, K., Viehweg, C., Stober, G., Kürschner, D., 2007. Adv. Space Res. 39 (8), 1278–1283. http://dx.doi.org/10.1016/j.asr.2007.01.003.

Janches, D., Brunini, C., Hormaechea, J.L., 2019. Astron. J. 157 (6), 240. http://dx.doi.org/10.3847/1538-3881/ab1b0f.

Janches, D., Close, S., Hormaechea, J.L., et al., 2015. Astrophys. J. 809, 36. http://dx.doi.org/10.1088/0004-637X/809/1/36.

Janches, D., Dyrud, L.P., Broadley, S.L., Plane, J.M.C., 2009. Geophys. Res. Lett. 36, 6101. http://dx.doi.org/10.1029/2009GL037389.

Janches, D., Swarnalingam, N., Carrillo-Sanchez, J., Gomez-Martin, J., Marshall, R., et al., 2017. Astrophys. J. 843, 11. http://dx.doi.org/10.3847/1538-4357/aa775c.

Jones, W., 1997. Mon. Not. R. Astron. Soc. 288 (4), 995–1003. http://dx.doi.org/10.1093/mnras/288.4.995.

Jones, J., Brown, P., 1993. Mon. Not. R. Astron. Soc. 265, 524–532. http://dx.doi.org/10.1093/mnras/265.3.524.

Kaiser, T., 1953. Adv. Phys. 2 (8), 495–544. http://dx.doi.org/10.1080/00018735300101282.

Kakac, S., Yener, Y., 1985. Heat Conduction, Vol. 65, No. 1, second ed. Hemisphere Publishing Corporation, p. 175. http://dx.doi.org/10.1002/cjce.5450650130, The Canadian Journal of Chemical Engineering.

Kohout, T., Kallonen, A., Suuronen, J.P., et al., 2014. M&PS 49 (7), 1157–1170. http://dx.doi.org/10.1111/maps.12325.

Liu, A.Z., Lu, X., Franke, S.J., 2013. J. Geophys. Res.: Atmos. 118 (4), 1668–1678. http://dx.doi.org/10.1029/2012JD018653.

Liu, X., Yue, J., Xu, J., et al., 2017. J. Geophys. Res.: Atmos. 122 (12), 6231–6249. http://dx.doi.org/10.1002/2017JD026604.

Lodders, K., Fegley, Jr., B., 2011. Chemistry of the Solar System. pp. 15–16.

Mazur, M., Pokornỳ, P., Brown, P., et al., 2020. Radio Sci. 55 (10), 1–31. http://dx.doi.org/10.1029/2019RS006987.

McKinley, D.W.R., 1961. Meteor Science and Engineering. McGraw Hill, New York, pp. 1–309.

Nawaby, B.S., Rochette, P., 2016. Acta Geophys. 64 (10), 1942–1969. http://dx.doi.org/10.1515/acgeo-2016-0055.

Nesvorný, D., Janches, D., Vokrouhlický, D., et al., 2011. Astrophys. J. 743, 129. http://dx.doi.org/10.1088/0004-637X/743/2/129.

Nesvorný, D., Jenniskens, P., Levison, H.F., et al., 2010. Astrophys. J. 713, 816–836. http://dx.doi.org/10.1088/0004-637X/713/2/816.

Öpik, E.J., 1958. Physics of Meteor Flight in the Atmosphere. Interscience Publishers, New York.

Panka, P.A., Weryk, R.J., Bruzzone, J.S., et al., 2021. Planet. Sci. J. 2 (5), 197. http://dx.doi.org/10.3847/PSJ/ac22b2.

Plane, J., 2003. Chem. Rev. 103 (12), 4963–4984. http://dx.doi.org/10.1021/cr0205309.

Plane, J.M.C., 2012. Chem. Soc. Rev. 41, 6507–6518. http://dx.doi.org/10.1039/c2cs35132c.

Pokorný, P., Vokrouhlický, D., Nesvorný, D., Campbell-Brown, M., Brown, P., 2014. Astrophys. J. 789, 25. http://dx.doi.org/10.1088/0004-637X/789/1/25.

Rowan-Robinson, M., May, B., 2013. Mon. Not. R. Astron. Soc. 429 (4), 2894–2902. http://dx.doi.org/10.1093/mnras/sts471.

Schult, C., Stober, G., Janches, D., Chau, J.L., 2017. Icarus 297, 1–13. http://dx.doi.org/10.1016/j.icarus.2017.06.019.

Schult, C., Stober, G., Keuer, D., Singer, W., 2015. Mon. Not. R. Astron. Soc. 450 (2), 1460–1464. http://dx.doi.org/10.1093/mnras/stv614.

Soini, A.-J., Kukkonen, I., Kohout, T., Luttinen, A., 2020. EGU General Assembly Conference Abstracts. p. 4679. http://dx.doi.org/10.5194/egusphere-egu2020-4679.

Stober, G., Brown, P., Campbell-Brown, M., Weryk, R.J., 2021. Adv. Appl. Probab. 654, A108. http://dx.doi.org/10.1051/0004-6361/202141470.

Stober, G., Jacobi, C., Singer, W., 2011. J. Atmos. Sol.-Terr. Phys. 73 (9), 895–900. http://dx.doi.org/10.1016/j.jastp.2010.06.009.

Stober, G., Janches, D., Matthias, V., et al., 2021. Ann. Geophys. 39 (1), 1–29. http://dx.doi.org/10.5194/angeo-39-1-2021.

Stober, G., Liu, A., Kozlovsky, A., et al., 2022. Atmos. Meas. Tech. 15 (19), 5769–5792. http://dx.doi.org/10.5194/amt-15-5769-2022.

Stober, G., Weryk, R., Janches, D., et al., 2023. Planet. Space Sci. 237, 105768. http://dx.doi.org/10.1016/j.pss.2023.105768.

Vondrak, T., Plane, J.M.C., Broadley, S., Janches, D., 2008. Atmos. Chem. Phys. 8, 7015–7031. http://dx.doi.org/10.5194/acp-8-7015-2008.

Webster, A.R., Brown, P.G., Jones, J., Ellis, K.J., Campbell-Brown, M., 2004. Atmos. Chem. Phys. 4 (3), 679–684. http://dx.doi.org/10.5194/acp-4-679-2004.

Weryk, R.J., Brown, P.G., 2012. Planet. Space Sci. 62, 132–152. http://dx.doi.org/10.1016/j.pss.2011.12.023.

Whipple, F.L., Jacchia, L.G., 1957. Smithsonian Contrib. Astrophys. 1, 183–206.

Zolensky, M., Bland, P., Brown, P., Halliday, I., 2006. In: Lauretta, D.S., McSween, H.Y. (Eds.), Meteorites and the Early Solar System II. p. 869.

Zook, H.A., 2001. Accretion of Extraterrestrial Matter Throughout Earth's History. pp. 75–92. http://dx.doi.org/10.1007/978-1-4419-8694-8_5.